

## Noninvasive manipulation of the optical response of opal photonic crystals

Sergei G. Romanov,<sup>1,3,\*</sup> Alois Regensburger,<sup>1</sup> Alexander V. Korovin,<sup>2</sup> Alexandra S. Romanova,<sup>1</sup> and Ulf Peschel<sup>1</sup>  
<sup>1</sup>*Institute of Optics, Information and Photonics, University of Erlangen-Nuremberg, Haber-Straße 9a, 91058 Erlangen, Germany*  
<sup>2</sup>*Lashkarev Institute of Semiconductor Physics NAS, pr. Nauki 41, Kiev, 03028, Ukraine*  
<sup>3</sup>*Ioffe Physical Technical Institute RAS, 194021, Politekhnicheskaya ul., 26, St. Petersburg, Russia*  
 (Received 4 February 2013; revised manuscript received 22 July 2013; published 13 September 2013)

The efficient manipulation with optical spectra of colloidal photonic crystals was achieved using the metal mirror positioned either immediately or at a distance from the crystal surface. If the mirror is close to the surface, the changes are mostly quantitative and relate to the improved light confinement. If the spacer provides a  $2\pi$  phase shift for round trip of the light at the wavelength of the diffraction resonance of the opal lattice, the defect band is formed in the photonic stop-band leading to 20–40 times increase of the transmission. The upper limit of the quality factor of the defect band was estimated by extrapolating the development of the defect transmission band as a function of the photonic crystal thickness. The specific features related to the photonic crystal dimensionality were revealed in the defect band spectra. The obtained results support the idea of achieving the control on the optical functionality of photonic crystals by recycling the transmitted light in the crystal volume.

DOI: [10.1103/PhysRevB.88.125418](https://doi.org/10.1103/PhysRevB.88.125418)

PACS number(s): 42.70.Qs, 78.67.Pt

### I. INTRODUCTION

Interference of incident and scattered waves in the lattice of finite size photonic crystals (PhC) determine their optical properties.<sup>1</sup> Conveniently, the modification of PhC optical properties is achieved by changing the refractive index contrast, the volume fraction, the shape, and the arrangement of nanostructures, which act as light scatterers. If crystals of finite size are considered, embedding lattice defects will also affect the response. Generalizing, the character of the optical response depends on the structure and the composition of photonic crystal. However, having the integrated photonic circuits in mind, these methods become impractical since fabrication of each functional PhC element would require the implementation of unique technological process.

In this paper, we address the feasibility of attaining different functionalities of finite size PhCs by making the crystal environment instrumental. To achieve this aim, we used the recycling of transmitted light in the same PhC. For example, such recycling was achieved in two-dimensional (2D) slab all-dielectric PhCs by attaching them to strongly reflecting metallized substrates. Subsequently, the modified optical response was interpreted in terms of enhanced light confinement and excitation of surface plasmon polaritons.<sup>2–4</sup> The obvious advantage of this method is that the structure and the composition of the PhC itself remain intact. This observation inspired our interest in implementation of the same approach to three-dimensional (3D) PhCs. In particular, the problem in question is how far one can change the optical response of popular opal-based PhCs by controlling the light coupling/decoupling at the crystal boundary.

The most desirable functional PhCs are those possessing the localized defect band inside the photonic band gap. Owing to the high Purcell factor, such defects facilitate the design of efficient light emitters and detectors. In this respect, the point (0D) defect in a 3D lattice appears the most advantageous configuration as the one providing the (3-0)D confinement. However, the technological complexity of defect formation dramatically escalates with increasing the PhC dimensionality.<sup>5</sup> That is why the planar defect in the

one-dimensional (1D) Bragg reflector is the most widely used defect in commercial optical devices, although it offers only the unidirectional (3-2)D confinement. In the case of a 3D PhC, the defects with 1D or 2D light confinement can offer resonator behavior or wave guiding. Some sophisticated architectures are also considered. For example, implanting a line defect in a planar 2D PhC, which is, in turn, embedded in 3D PhC with an omnidirectional band gap, was proposed as a route for achieving a lossless PhC waveguide.<sup>6</sup>

Opal films are frequently studied 3D PhCs assembled from colloidal beads<sup>7</sup> [Fig. 1(a)]. The drawback of opal-based PhCs is the fixed lattice topology, which cannot be changed without the aid of external templates.<sup>8</sup> Correspondingly, the optical response of such PhCs demonstrates poor variability. To overcome this limitation, the attention was turned to opals with embedded defects. The defects can be built in the opal volume either due course of crystal assembling<sup>9,10</sup> or formed by means of postcrystallization processing, e.g. using electron beam lithography or two-photon polymerization technique.<sup>11,12</sup> However, the lattice irregularities of currently available self-assembled opals make the incorporation of artificial wavelength-size 1D and 0D defects almost senseless, since the respective defect modes will be lost in a pool of intrinsic defect modes. This consideration justifies the current interest to planar defects, the optical response of which can be easily detected.

The common approach to introducing planar defects in opals exploits the idea of heterostructuring.<sup>9,13–16</sup> It assumes crystallization of the opal film, preparation of the defect layer, and subsequent resuming of the opal growth to produce the sandwichlike structures. The shortcoming of such a multiple-step method is likely a lateral misalignment of sequentially crystallized 3D lattices. The corresponding mismatch of the electromagnetic (EM) field distributions can be the reason for poor resolution of defect bands reported in the literature to date.

In this work, we assembled thin film opals on a dielectric substrate precoated with a semitransparent metal film. This approach is a part of the strategy leading to hybrid metal-dielectric PhCs, in which the light is carried by photons and

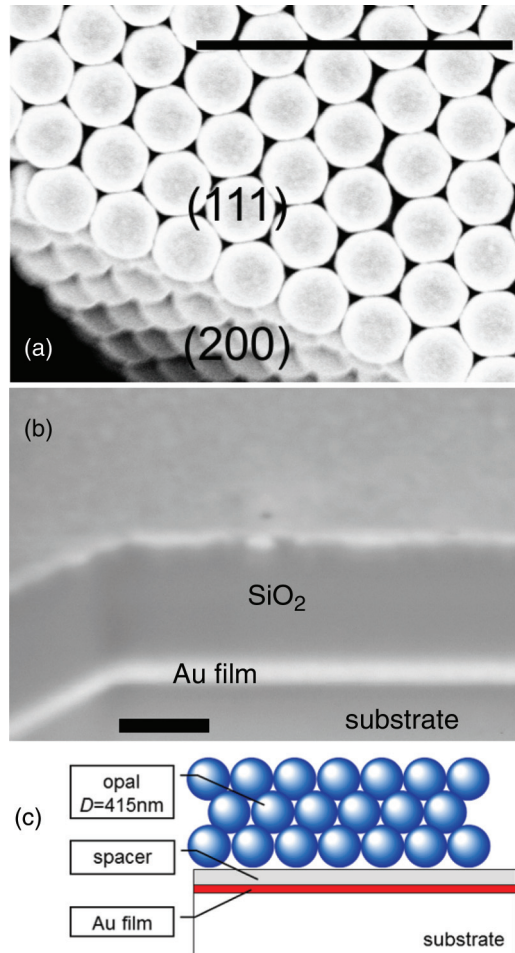


FIG. 1. (Color online) (a) SEM image of the opal film. Scale bar—2  $\mu\text{m}$ . (111) and (200) planes are seen. (b) SEM image of the cross-section of the substrate with deposited thin gold film and a dielectric spacer on top. Scale bar—200 nm. (c) Schematics of the opal-spacer-Au hybrid PhC.

plasmons.<sup>17,18</sup> From the practical point of view, monolayers of spheres on a gold substrate were used to enhance the sensitivity of gas detection<sup>2</sup> and to increase the brightness of embedded light sources.<sup>3</sup>

If opal is assembled on a transparent substrate, the intensity of light that is reflected back in its volume at the opal-substrate boundary is low, and its influence on the field distribution in the opal volume can be neglected. In the case of the metal mirror-terminated opal, the intensity of reflected light is high that brings a noticeable change of colors of thin film opals.<sup>19</sup> The first aim of this paper is to characterize the spectrum transformation occurring due to such recycling of light.

The next task is to exercise the control on the light recycling. Towards this aim, we considered the phase shift of light, which is back reflected by the metal mirror, by means of a spacer inserted between the metal film and the opal. Opal lattice is commonly described as the face-centered cubic (fcc) lattice of touching spheres,<sup>20</sup> but along the film normal the opal crystal can be regarded as the stack of (111) growth planes that are parallel to the substrate. Hence, the studied architecture can be considered similarly to a resonant cavity, which is embedded between the metal and the Bragg mirrors.<sup>21,22</sup> We

reduced the spacer thickness to a fraction of a wavelength and tuned its thickness to provide a multiple  $2\pi$ -large phase shift for light performing a round trip at the frequency of the (111) diffraction resonance. This approach effectively mimics the functionality of the defect band inside the photonic stop-band.

In the 3D lattice, the incoming light beam is expanded in a number of diffraction orders for each of the differently oriented crystal planes. Moreover, the spectral density of resonances increases along the wavelength decrease. The lattice symmetry also reveals itself as a spatial anisotropy of the optical response for the same wavelength. Moreover, different diffraction resonances possess different dispersions, which can intersect each other leading to the multiple-wave diffraction. Eventually, multiple defect modes can be produced at such conditions. This is a true 3D effect, which can be used as a benchmark for testing light recycling in the conditions of avoided band crossings.<sup>23,24</sup>

The external control over the defect mode faces the limitation of the opal film thickness. On the one hand, the Bragg mirror should be thick enough to confine light in a microcavity. On the other hand, it should be thin enough to ensure coupling light to the cavity. This makes the number of (111) layers in the opal film the important parameter that provides a balance between light localization and crystal transparency. Towards this aim, we compared resonant architectures assembled using colloidal crystal films of different thicknesses and demonstrated that the spectrum of a defect band depends on the PhC dimensionality, and the observed quality factor saturates with the increase of the Bragg mirror thickness.

## II. EXPERIMENTAL TECHNIQUE

A glass slide was coated with 30-nm-thick Au film, which was subsequently protected by the 15-nm-thick SiO<sub>2</sub> layer, using the magnetron sputtering in high vacuum conditions. This protection layer provides also the hydrophilic conditions necessary for opal self-assembly. If the thickness of a SiO<sub>2</sub> layer is increased to the hundreds of nanometers, it can be used as the  $\frac{1}{4}$ -,  $\frac{1}{2}$ -, and so on wavelength resonator in the visible part of spectrum [Fig. 1(b)].

The opal films were subsequently crystallized on such substrates in a moving meniscus from a suspension of 415-nm polymethylmethacrylate (PMMA) spheres [Fig. 1(c)] under the white noise agitation.<sup>25</sup> In what follows, the opal film thickness will be referred to using the number of hexagonally packed monolayers of spheres, which are parallel to the substrate. Using (hkl) Miller indices, these are the (111) planes of the fcc lattice. The thickness of opal films in studied samples is varied from 1 to 10 of such layers. The structure without a resonator will be called the opal-Au (O-Au) hybrid, and the one with the resonator, the opal-resonator-Au (O-R-Au) hybrid. In this work, we used a 280-nm-thick spacer.

Angular-resolved transmission and reflectance spectra were obtained under the white light illumination using a collimated 1-mm-diameter beam from a tungsten lamp. The measurements were performed with linearly polarized light by placing the sample between the polarizer and the analyzer. Coplanar orientation of polarizing elements was chosen so

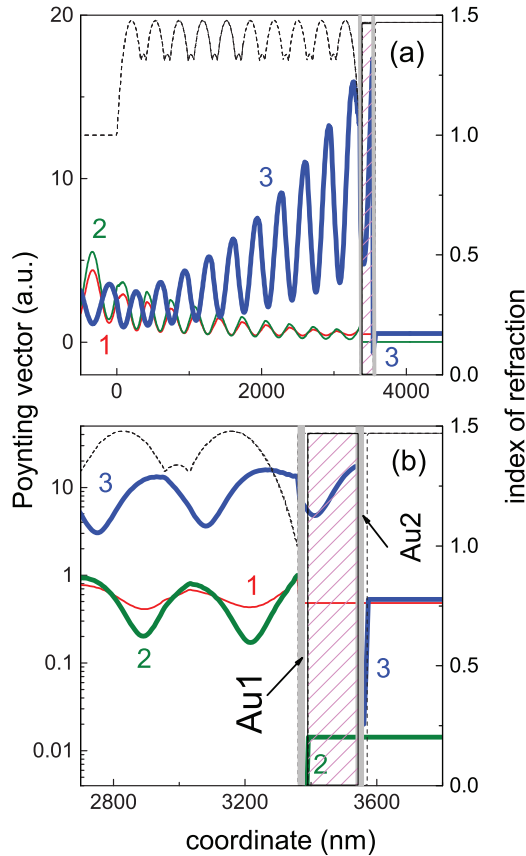


FIG. 2. (Color online) The in-plane components of the Poynting vector in  $p$ -polarized light across the 10-layer-thick (10L) Bragg mirror in the center of its stop-band for (curve 1) the Bragg mirror on a glass substrate, (2) the Bragg mirror on Au film coated glass substrate, and (3) at the wavelength of the defect band for the Bragg mirror-resonator-Au-coated glass substrate. Thin dashed line shows the refractive index profile of these structures. The resonator cavity is shown by a shaded box. Au1 and Au2 denote Au films in Bragg-Au and Bragg-R-Au cases, respectively.

that the data correspond to coupling the  $s$ - (or  $p$ -) polarized incident light to  $s$ - ( $p$ -) polarized transmitted or reflected light. The scrambler plate was used in front of the entrance slit of the spectrometer. Angular-dependent spectra were acquired in the range from  $0^\circ$  ( $6^\circ$  in the case of reflectance) to  $80^\circ$  of the beam inclination with respect to the film normal  $\theta$ , with the step down to  $1^\circ$ .

For the sake of interpretation, we compared our experimental results with the model structure consisting of a 1D Bragg mirror that is separated by a spacer from the semitransparent metal mirror. The transfer matrix method was used to model the response of the 1D Bragg mirror, which was assumed to be a stack of 10 dielectric layers, a cross-section of which mimics the refractive index profile of the opal lattice along its  $[111]$  axis [Fig. 2(a)].<sup>26</sup> The transmission/reflectance spectra and the field distributions of this Bragg multilayer were calculated for three model structures, namely, (i) the Bragg mirror on a glass substrate, (ii) the Bragg mirror on 30-nm Au film on a glass substrate, and (iii) the Bragg mirror on  $\frac{1}{4}$ -wavelength resonator on 30-nm Au film on a glass substrate.

### III. OPAL ON A METAL MIRROR

The profile of the Poynting vector across the Bragg mirror was calculated at the center of the stop-band for oblique light incidence at  $\theta = 10^{-5^\circ}$  [Fig. 2(a)]. One can see that EM flux magnitude drops in depth of the Bragg stack.

The spectra of the Bragg mirror demonstrate the stop-band and Fabry-Perot oscillations [Figs. 3(a) and 3(b)]. In the  $p$ -polarized light, the reflectance approaches a minimum at the Brewster angle  $\theta_B \approx 56^\circ$  for off-resonance wavelengths, whereas the Bragg reflectance band almost disappears at the critical angle of diffraction  $\theta_c \approx 62^\circ$  (Ref. 27) [Fig. 3(b)]. By crossing this angle range, the phase of substrate-reflected light experiences  $\pi$ -large shift at the Brewster angle, whereas the phase of light reflected at interlayer interfaces in the Bragg mirror experiences the same shift at the critical angle. As a result, the Bragg resonance disappears in between these angles, but comes back at higher angles when the phase correlation is restored.

The same structure with the 30-nm Au film in between the Bragg mirror and the glass substrate (Bragg-Au) possesses substantially lower transmission, similar stop-band, and sharper Fabry-Perot oscillations owing to the higher reflectance of the substrate [Figs. 3(c) and 3(d)]. No dramatic changes of  $s$ -polarized transmission are introduced by adding a thin Au film, except transmission reduction in proportion to the metal film transmittance and the relative increase of the height of Fabry-Perot oscillations. Calculations of the Poynting vector show that the in-plane  $p$ -polarized energy flux remains almost the same [Figs. 2(a) and 2(b)]. However, there is a strong distinction from the case of a Bragg mirror on a dielectric substrate in the form of changing the sign at the metal-substrate interface, which is a qualifying property of the surface plasmon polariton.<sup>28</sup> Thus, plasmonic excitations take part in the light transfer in such architectures.

In contrast to transmission, the reflectance map of the Bragg-Au hybrid for  $p$ -polarized light is qualitatively different from its counterpart on a dielectric substrate [compare Fig. 3, panels (b) and (d)]. The pseudo-Brewster angle for the metallized substrate is not approached in the studied angle range; hence, the corresponding minimum is cancelled, but the phase shift at the critical angle is preserved. As a result, the interference pattern experiences the  $\pi$ -large phase shift at the critical angle, and the diffraction maximum is replaced by the diffraction minimum. The same applies to Fabry-Perot oscillations. This observation illustrates the feasibility of the external control on the optical response of photonic crystals.

Replacement of the Bragg mirror with the opal reflector reproduces, in general, the differences between spectra of Bragg-glass and Bragg-Au-glass structures. At the normal beam incidence, the transmission spectrum of the opal-glass sample shows the (111) diffraction resonance centered at 915 nm and the degenerate diffraction resonances from (222), (220), and (200) planes around 470 nm [Fig. 4(a), curve 1]. The complementary (111) diffraction peak occurs in the reflectance spectrum [Fig. 4(b), curve 1]. If the opal film is assembled on Au film, the transmission is decreased by a factor of 10, the resonances in transmission spectrum of O-Au hybrid remain qualitatively the same as in the opal film on glass, but the transmission spectrum is superimposed on a

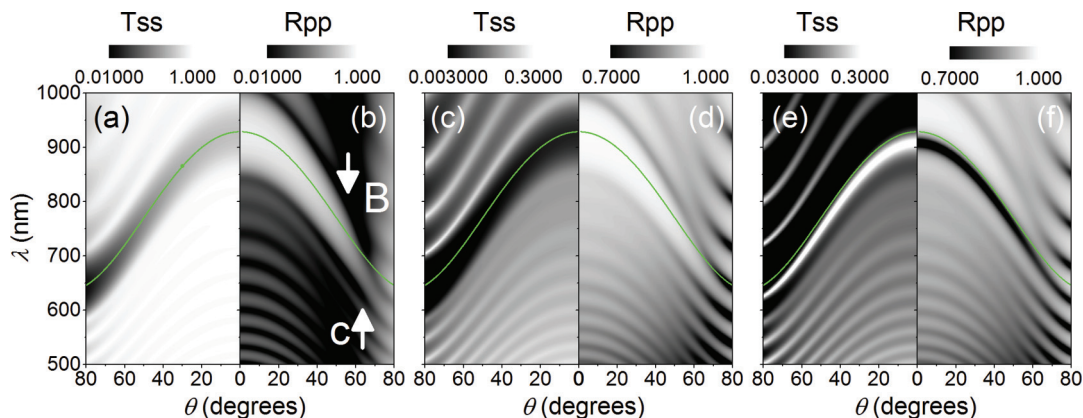


FIG. 3. (Color online) (a) Calculated  $s$ -polarized transmission spectra of the Bragg mirror on (a) glass substrate, (c) 30-nm Au-coated glass substrate, and (e)  $\frac{1}{4}\lambda$  resonator on 30-nm Au-coated glass substrate. (b), (d), and (f) Calculated  $p$ -polarized reflectance for the same structures. Dispersion of the Bragg resonance in the Bragg mirror is shown on all panels to guide the eye. In panel (b), arrows mark the positions of the Brewster angle and the critical angle of diffraction.

background, which follows the transmission of the metal film [Fig. 4(a), curves 2 and 4]. The transmission drop at 512 nm in the spectrum of Au film indicates the onset of interband transitions in gold itself (curve 4).<sup>29</sup>

In the  $s$ -polarized transmission spectra of the O-Au hybrid, the diffraction resonances of the opal lattice are preserved in the broad range of incidence angles [Figs. 5(a) and 5(c)]. The departure of dispersions of diffraction resonances at high (hkl) index planes from that calculated for the perfectly packed fcc lattice of spheres (lines in Fig. 4) can be explained by slight stretching of the opal lattice along the direction of pulling the substrate out of sphere suspension during crystallization.<sup>30</sup>

The reflectance spectra experience stronger alterations. The diffraction resonances at high Miller index planes appear

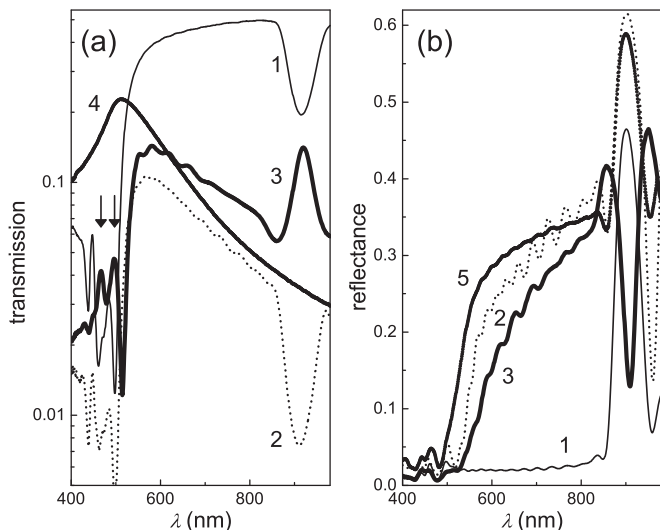


FIG. 4. (a) Transmission spectra of the (1) bare opal [9 (111) planes comprising the opal film], (2) O-Au hybrid [10 (111) planes], (3) O-R-Au hybrid [9 (111) planes] and (4) 30-nm Au film at  $\theta = 0^\circ$ . (b) Reflectance spectra of (1) bare opal, (2) O-Au hybrid, and (3) O-R-Au hybrid acquired at  $\theta = 6^\circ$ . The spectrum  $R_{\text{opal-Au}} = R_{\text{opal}} + 0.7T_{\text{opal}}$  (curve 5) is shown for reference. Arrows show the defect transmission bands supported by high (hkl) plane resonances.

as minima in mirror reflectance spectra of the O-Au hybrid [compare Figs. 6(a) and 6(c)]. We argue that reflectance spectra of the O-Au hybrid can be represented as the sum of transmission and reflectance spectra of the same opal film on a dielectric substrate [compare curves 2 and 5 in Fig. 4(b)]. The reason for such superposition is the metal film, which reflects the transmitted light back in the opal volume. Other differences are the  $\sim 10$ -fold enhancement of the magnitude of Fabry-Perot oscillations [curve 2, Fig. 4(b)] and the cancellation of the Brewster minimum in  $p$ -polarized reflectance spectra [Fig. 6(d)].

In agreement with the Bragg mirror model, the transmission and reflectance patterns of O-Au hybrid in  $p$ -polarized spectra show the inversion of Fabry-Perot oscillations and (111) diffraction resonance at incidence angles higher than the critical one [Figs. 5(d) and 6(d)]. Remarkably, since the lattice disorder almost diminishes the difference between the Brewster and critical angles in the opal film,<sup>27</sup> the replacement of the Bragg maximum with the minimum in reflectance occurs at  $\theta \approx 58^\circ$ . Thus, recycling of transmitted light by highly reflecting metallized substrate results in the higher off-resonance reflectivity and the inversion of resonances at high angles of light incidence.

#### IV. OPAL ON A RESONANT CAVITY

The dielectric spacer between the metal and Bragg mirrors is able to control the phase shift of recycled light. This spacer can be turned into a resonance cavity, if the light acquires the integer multiple of  $2\pi$  phase shift for the round trip over the metal mirror, the cavity, and the Bragg mirror. For example, the  $\frac{1}{4}$ -wavelength cavity provides the  $\pi$  phase shift at the  $\lambda_{\text{Bragg}}$ , if its optical path length is  $\lambda_{\text{Bragg}}/(4n_r)$ , where  $\lambda_{\text{Bragg}}$  is the resonance frequency of the Bragg mirror, and  $n_r$  is the refraction index of the spacer material. Simulated transmission spectra of hybrid architecture with the cavity resonance at  $\lambda_{\text{Bragg}}$  show the transmission peak occurring inside the photonic stop-band and the complementary dip in reflectance spectra [Figs. 3(e) and 3(f)]. Remarkably, the

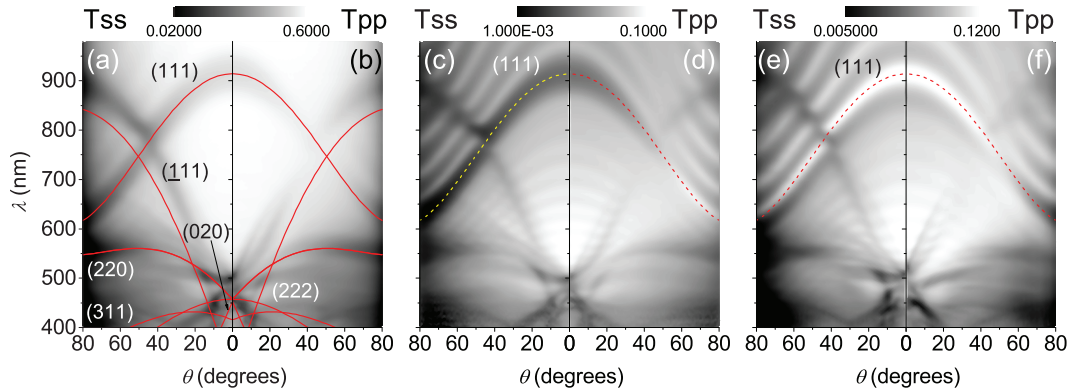


FIG. 5. (Color online) Transmission spectra in *s*- and *p*-polarized light of (a) and (b) opal film, (c) and (d) O-Au, and (e) and (f) O-R-Au samples. The transmission intensity is plotted in the logarithm scale. Lines show the dispersion of diffraction resonances in the fcc lattice. The Miller indices of diffracting planes are shown at curves. The misalignment of projected band dispersions and measured diffraction minima occurs due to distortion of the opal lattice.

defect transmission greatly exceeds that outside the Bragg stop-band.

The reason for such spectral changes is strong modification of the EM field at the resonance in the structure. The resonant cavity reverses the distribution of the EM flux; it now increases from the outer surface of the Bragg mirror towards the cavity in contrast to architectures without the resonator (Fig. 2). This is a typical functionality of the localized mode inside the photonic bandgap.<sup>1</sup> What is different from the nonmetallic structures is the hybrid character of the resonant mode. In Fig. 2(b) one can see the asymmetric shape of the Poynting vector profile in close vicinity to the resonator, which manifests the superposition of the photonic crystal and surface plasmon polariton modes. The opposite directions of the surface plasmon polariton propagation at the cavity-metal and metal-substrate interfaces is another evidence of plasmon contribution to the defect mode transmission in this case.

The dispersion of the defect band in reflectance strictly follows the dispersion of the defect peak in transmission. Notably, the Fabry-Perot pattern of the Bragg-R-Au structure unevenly differs from that of the Bragg-Au hybrid [compare panels (d) and (f) in Fig. 3] because the spectral position of these resonances now depend on the phase difference acquired in the cavity.

In the experiment, the defect mode of the O-R-Au hybrid emerges at the place of the (111) diffraction minimum in the transmission spectrum of the opal film [curve 3, Fig. 4(a)]. Accordingly, the dip partly replaces the band in the reflectance spectrum [curve 3, Fig. 4(b)]. The width of a defect band in opal-based samples greatly exceeds that in model Bragg mirror spectra. Most probably, this difference can be assigned to both the poor approximation of the sphere crystal by continuous dielectric layers and to the light scattering at intrinsic lattice defects. Nevertheless, the quality factor of this resonance band is  $\sim 20$ . For comparison, if the cavity is inserted between two opal films, the defect transmission band comprises about 50–70% of the (111) minimum depth.<sup>10,16,31</sup> Thus the observed  $\sim 10$ -fold increase of transmission in a defect mode of the O-R-Au hybrid is far superior over that in opal-defect-opal architectures.

If the cavity resonance matches the central wavelength of the Bragg resonance, the transmission peak is accompanied by the side dips (or bands in reflectance), i.e. the bandwidth of the cavity resonance is smaller than that of the diffraction one. By changing the cavity thickness, the resonance band moves toward the edge of the diffraction minimum and becomes less pronounced (Fig. 7). The fact that the defect band disappears, if detuning of the cavity

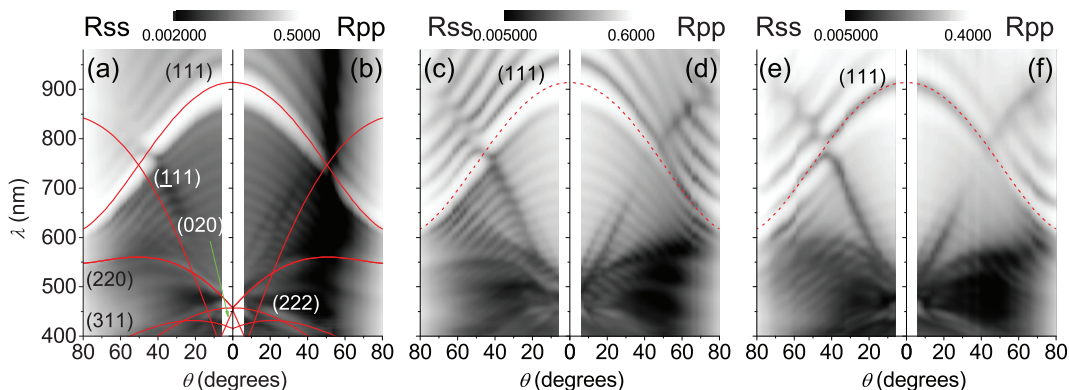


FIG. 6. (Color online) Reflectance spectra in *s*- and *p*-polarized light of (a) and (b) opal film, (c) and (d) O-Au, and (e) and (f) opal-R-Au samples. The reflectance intensity is plotted in the logarithm scale.

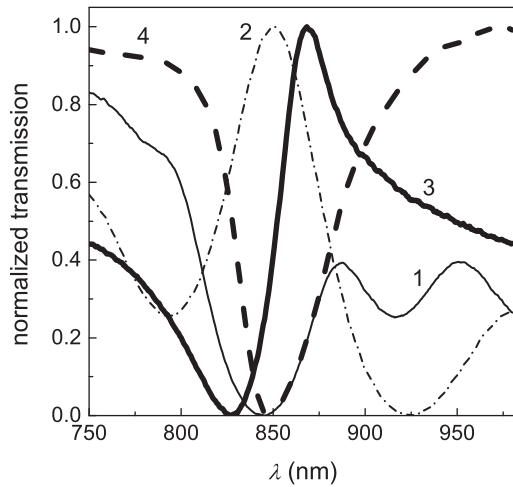


FIG. 7. (Curve 1) Normalized *p*-polarized transmission of O-Au and (curves 2, 3, and 4) O-R-Au hybrids with different cavity thicknesses obtained at  $\theta = 30^\circ$ .

length exceeds  $\pm 5\%$  range with respect to the (111) diffraction resonance, agrees with the model calculations with the Bragg mirror.

Interestingly, in *p*-polarized light at  $\theta > \theta_B$ , the defect transmission band of O-R-Au hybrid turns into the minimum and the defect reflectance dip into the maximum, but no such changes are observed for *s*-polarized light. This behavior is opposite to the (111) resonance appearance in O-Au hybrid

and agrees with the  $\pi$ -phase shift provided by the cavity to the recycled light at the resonance wavelength.

No evidence of plasmonic modes was observed in spectra of studied hybrid samples in contrast to the case of the monolayer of spheres on a metal film,<sup>2-4</sup> although opal ought to provide efficient grating coupling of light to surface plasmon polaritons. Two reasons can be mentioned here: (i) the surface plasmon polaritons are localized in the vicinity to the opal-resonator interface as follows from the field distribution in the Bragg-R-Au hybrid (Fig. 2), and (ii) both the diffracted and scattered in the opal film light induce surface plasmon polaritons, and individual modes cannot be resolved over such a background.<sup>32</sup>

**V. EFFECTS OF THE OPAL LATTICE DIMENSIONALITY**

In the O-R-Au hybrid the primary Bragg mirror is the stack of (111) monolayers, 0th diffraction order of which propagates along the mirror reflectance direction in our experimental set up. However, the 3D opal lattice possesses different crystal planes in contrast to the one set in the multilayer Bragg stack. Correspondingly, the transmission maps of the multilayered stack and the opal film look different (compare Figs. 3 and 5). Obviously, 0th diffraction orders of all other (hkl) planes propagate at the angle to the 0th order of (111) diffraction. The reasonable question is whether these resonances will be affected by the light recycling?

Such a situation can be realized, e.g. if the incident light possesses the wave vectors that are equal to the distance from the center to the edges of the first Brillouin zone, where

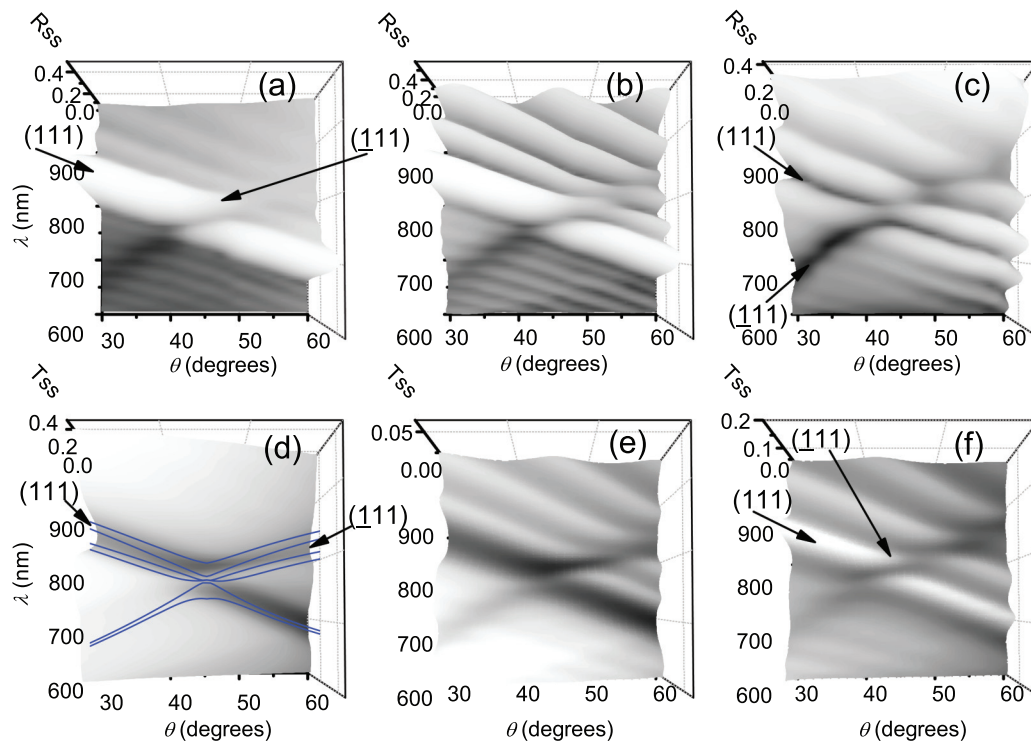


FIG. 8. (Color online) (a)–(c) Reflectance and (d)–(f) transmission spectra of the opal film, O-Au, and O-R-Au samples, respectively, in *s*-polarized light. The fragment of the photonic bandgap diagram of the opal crystal calculated using the plane wave expansion method overlays the transmission plot in panel (d) for reference (Ref. 35). Arrows labeled by Miller indices point to the diffraction resonances at respective crystal planes.

the diffraction conditions are satisfied simultaneously for two different crystal planes. For example, these are the  $\Gamma U$  and  $\Gamma K$  directions, which correspond to collinear propagation of 0th diffraction orders for (111) and (200) or (111) and  $(\bar{1}11)$  planes, respectively, occurring at  $\theta = 42^\circ$  (see inset to Fig. 9). Along these directions, the multiple wave diffraction results in the avoided band crossings of the dispersion of diffraction resonances in  $s$ -polarized light [Figs. 8(a) and 8(d)] so that the Bragg mirror is discarded in the respective wavelength range [inset Fig. 8(d)].<sup>24</sup>

The metal mirror does not change the anticrossing of diffraction resonances in the case of the O-Au hybrid [Figs. 8(b) and 8(e)]. In addition, anticrossings appear at intersections of the  $(\bar{1}11)$  resonance with Fabry-Perot modes, pointing to their similarity with (111) diffraction resonance.

In the case of the O-R-Au hybrid, the appearance of the avoided band crossing is opposite to that in the O-Au hybrid. In reflectance, it looks like the anticrossing of two diffraction minima, whereas in transmission, it looks like the anticrossing of two transparency bands [Figs. 8(c) and 8(f)]. Qualitatively, the reflectance map of O-Au hybrid is replaced with the transmission map of O-R-Au hybrid and vice versa [compare panels (b) with (f) and (e) with (c) in Fig. 9]. Importantly, within the width of the cavity resonance, it is possible to trace the defect bands along the dispersion of  $(\bar{1}11)$  resonance. This observation confirms a multiple  $2\pi$ -phase shift for the round trip at the resonance wavelength of the  $(\bar{1}11)$  Bragg mirror.

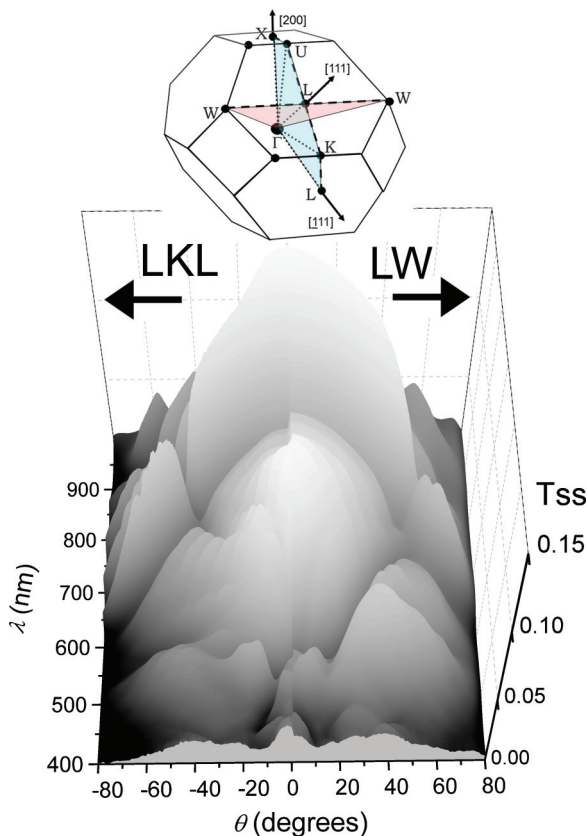


FIG. 9. (Color online) Directionality of the O-R-Au hybrid transmission spectra obtained in  $s$ -polarized light. Inset shows the Brillouin zone of the fcc crystal and depict two cross-sections of this zone associated with measured spectra.

In 3D PhCs, an electromagnetic field is structured in Bloch modes, and in general, the field composition in Bloch modes changes with the direction of light propagation.<sup>33</sup> In particular, these modes are different in the most popular orientations of the plane of incidence, which relate to the  $\Gamma LKL$ ,  $\Gamma LUX$ , and  $\Gamma LW$  cross-sections of the Brillouin zone (inset in Fig. 9). Consequently, it is not surprising that transmission diagrams of the O-R-Au hybrid acquired by scanning along  $LKL$  and  $LW$  lines (Fig. 9) show not only the different patterns of resonances, but also the different behaviors at the intersection of photonic bands.

Owing to the symmetry of the fcc crystal, there are no avoided band crossings for the  $\Gamma W$  wave vectors (the vertices of the Brillouin zone), which relate to the simultaneous diffraction at (111), (200), and  $(\bar{1}11)$  sets of crystal planes. Clearly, the (111) defect band in  $s$ -polarized light remains continuous for scanning along the  $LW$  line because (200) and  $(\bar{1}11)$  diffraction resonances apply weak minima to the band profile at  $\theta = 53^\circ$ . This observation tentatively links the defect band appearance to the EM field distribution in Bloch modes of the 3D opal mirror.

## VI. DEVELOPMENT OF A DEFECT BAND

The exponential drop of the electromagnetic energy flow away from the cavity [Fig. 2(a)] assumes that the light localization can be achieved using the Bragg mirror with a relatively small number of diffracting layers. In order to verify this tendency, we studied the development of the defect band in transmission spectra of the O-R-Au hybrid along the increase of the number of (111) planes in the opal film. This number is equal to the number of Fabry-Perot oscillations between (111) and (222) resonances, as it postulated for multilayered systems.<sup>34</sup>

The overview of transmission maps of O-R-Au architectures in Fig. 10 shows the common feature—the transmission minimum at 510 nm for the normal light incidence. In the case of the monolayer coating, this minimum manifests the excitation of a waveguide mode at wavelength  $\lambda \approx n_{\text{eff}} D$ , where  $n_{\text{eff}}$  is the effective index of refraction of the colloidal crystal, and  $D$  is the diameter of the sphere.<sup>4,35,36</sup> The same feature is preserved in transmission spectra of the opal, as was noticed earlier,<sup>37</sup> where it coincides with the degenerate diffraction resonances at (222), (200), and (220) planes for the normal light incidence.<sup>38</sup> The actual diffraction pattern of the opal lattice [see dispersion lines in Fig. 5(a)] becomes evident for self-assembled colloidal crystals with more than 4 monolayers in thickness, where the A-B-C sequence of (111) planes of the fcc lattice can be realized.

In the long wavelength range, all these transmission patterns show the transmission band, which was identified as the band of defect transmission in the preceding discussion of 9 (111) plane-thick O-R-Au hybrid. Remarkably, the same band can be traced down to the 1-monolayer-thick coating with projected resonance wavelength  $\sim 1000$  nm at  $\theta = 0^\circ$ . Since 1-layer colloidal coatings cannot provide diffraction, this defect band should be associated with the Fabry-Perot resonance, which corresponds to the thickness of the colloidal monolayer  $\lambda \approx 2n_{\text{eff}} D$ . The sample with a 2-layer coating shows, at the normal light incidence, the maximum centered

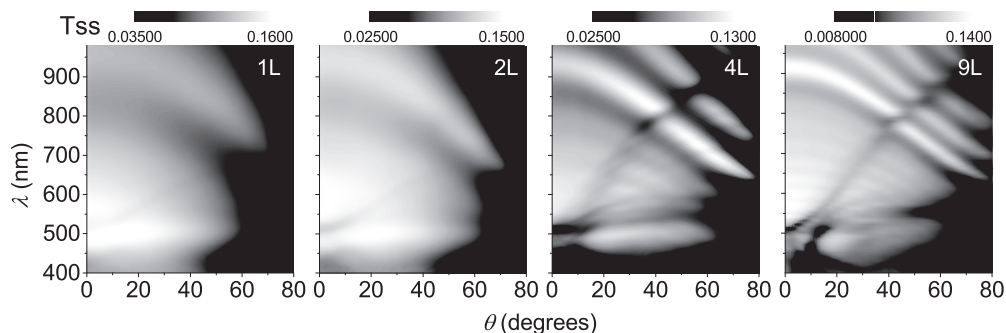


FIG. 10. Development of the defect transmission band and diffraction bands in the colloidal crystal-resonator-Au hybrid architectures followed the increase of the number of monolayers of spheres as demonstrated by transmission maps for the  $s$ -polarized light. Changing from 2D slab to 3D fcc crystal diffraction takes place when the number of monolayers  $N > 3$ .

at  $\sim 980$  nm and two subsequent minima at, approximately, 670 and 510 nm, all of which are the Fabry-Perot resonances that are equidistantly spaced along the frequency axis. The same regularity applies to 4- and 9-layer samples. Mie resonances of spheres as sources of light scattering can be disregarded from consideration since, for 430-nm spheres, their dipole resonance appears at  $\sim 700$  nm.

The fact that the defect band appears qualitatively the same for colloidal crystals of different dimensionality is the result of achieving the necessary phase shift for the light round trip independent upon whether the mirror action is provided by the Fabry-Perot or by the diffraction resonances. The specificity of the 3D crystals is the emergence of the avoided band crossing for thicker colloidal coatings.

With increasing the number of (111) planes  $N$ , the Bragg resonance gradually drifts to shorter wavelengths [Fig. 11(a)]. Assuming the same reflectivity of the metal mirror, this shift can be associated with the increasing reflectivity of the colloidal crystal. If the reflectivity is low, the effective thickness of the resonator exceeds the cavity thickness. Along the increase of a number of (111) layers, the effective resonator thickness converges to the geometric cavity thickness. To some degree, this blueshift is counteracted by the densification of the colloidal crystal, leading to the increase of its effective refractive index. Applying the asymptotic fit to the experimental points, we derived the value  $\lambda_c \approx 900$  nm to which the resonance converges for  $N > 50$ .

The transmission in a defect band maximum is proportional to the Bragg reflectivity of the colloidal crystal. We defined the transmission enhancement factor as the ratio of the transmission at the defect band maximum to that at its bottom [Fig. 11(b)] and fitted its dependence on the number of layers using the expression of the Bragg mirror reflectivity  $R = a/[1 + b/sh^2(cN)]$ ,<sup>34</sup> where  $a, b$ , and  $c$  are fitting parameters. The enhancement factor saturates at  $N > 50$ .

The resolution of the defect band is characterized by the quality factor obtained as the inverted full bandwidth at the half height [Fig. 11(c)]. Applying the fit in the form  $Q = Q_c[1 - \exp(-N/N_c)]$ , we obtained the saturation limit of  $Q_c \approx 33$  for the same  $N > 50$ .

It is worth noting that quoted values are specific to the reflectivity of the metal mirror and ordering of the colloidal crystal. In order to achieve the smooth curves, we used the data obtained with the wedged opal film. Changing the opal

crystallization protocol, e.g. the concentration of suspension or the speed of substrate drawing, results in noticeable deviation of the diffraction resonance strength from sample to sample for the same number of (111) layers.

## VII. INTERFACE FUNCTION

Transmission maps of O-R-Au hybrids possess a large number of resonances, which makes it difficult to distinguish the effect of light recycling (see, e.g. Fig. 9). In order to explicitly demonstrate the changes introduced by the resonant microcavity, we constructed the so-called interface function, which is the ratio  $T_{ss,pp}^{\text{opal-R-Au}}/T_{ss,pp}^{\text{opal-Au}}$  [Figs. 12(a) and 12(b)]. For the sake of correctness, one should compare the spectra of O-R-Au and O-Au samples with the same number of

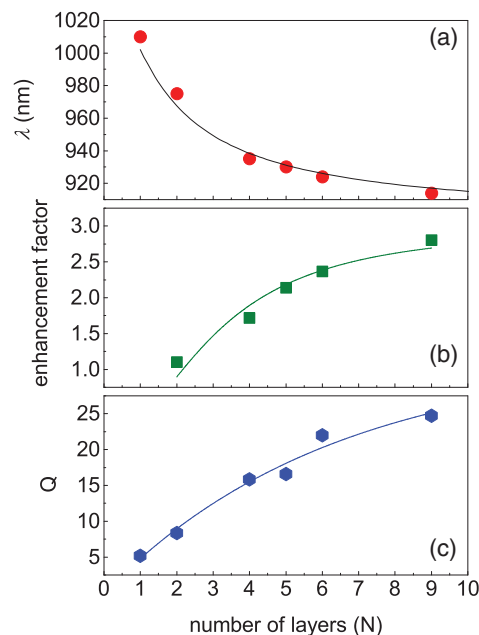


FIG. 11. (Color online) Circles, squares, and hexagons show, respectively, (a) the wavelength of the defect transmission band maximum, (b) the relative magnitude of the defect band, and (c) the quality factor of the defect band as a function of the number of monolayers of sphere comprising the colloidal crystal films. Lines represent asymptotical fits discussed in the text.

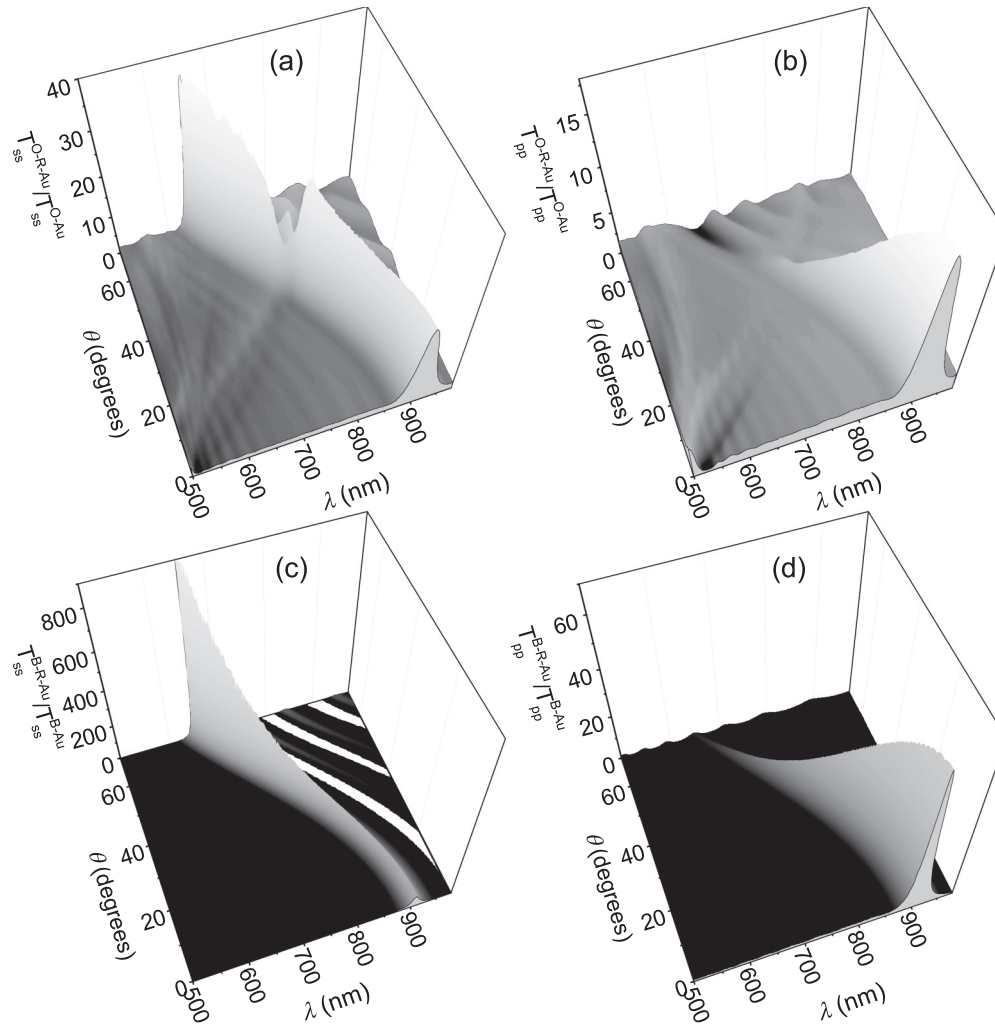


FIG. 12. Spectra of defect transmission as revealed by interface functions for (a) and (b) the O-R-Au hybrid architecture and (c) and (d) the Bragg-R-Au in  $s$ - and  $p$ -polarized light, respectively.

(111) planes in each hybrid. Expectedly, the major feature of this function is the peak aligned with the (111) resonance. The magnitude of the interface function peak increases with the increase of the incidence angle in  $s$ -polarized light and decreases in  $p$ -polarized light. At the normal light incidence, the defect mode transmission is  $\sim 20$  times higher compared to the transmission in the stop-band of the O-Au hybrid.

Comparing to interface functions of the computed 10-layer-strong Bragg-R-Au model, one can notice that the shape, the dispersion, and the polarization anisotropy of the interface function of the O-R-Au hybrid follow the simulated example. Noticeably, the interface function peak in simulations is higher than the experimental one. This difference accumulates the effectively stronger reflectance of continuous diffracting layers, the scattering losses occurring at defects of the opal lattice, and scattering due to irregularities of the microcavity.

Remarkably, the interface function also reveals the transmission enhancement peak occurring in the range 450–500 nm (Fig. 13). Judging from the band dispersion, this peak corresponds to the diffraction resonances at (222) and (220) planes [see dispersions in Fig. 5(a)]. The related transmission

minima at 465 and 496 nm in opal and O-Au hybrid and transmission peaks in O-R-Au hybrid are marked by arrows in Fig. 4(a). Such correspondence means that these resonances are also affected by the recycled light, and the  $2\pi$ -multiple phase shift applies to the round trip at their wavelengths. The narrow angle range and lower fivefold transmission increase for the second cavity harmonic can be explained by weak appearance of the (222) diffraction minimum in opal spectra, higher defect scattering at shorter wavelengths, and poor reflectivity of the gold film due to its intrinsic absorption at  $\lambda < 510$  nm [Fig. 4(a)].

The development of the interface function with increasing number of monolayers in colloidal crystal (Fig. 14) summarizes the cavity-related transmission changes. First of all, the transmission enhancement at the cavity resonance wavelength appears independently on packaging of the colloidal crystal. The eigenmode structure of 2-monolayer-thick crystal is the direct analogy to that of 1-monolayer crystal (Fig. 10). Nevertheless, its interface function demonstrates the broad but well-resolved-over-the-background dispersive band of defect transmission [Fig. 12(a)]. This band is of the same type as the defect band of a 3D O-R-Au hybrid [Fig. 14(c)].

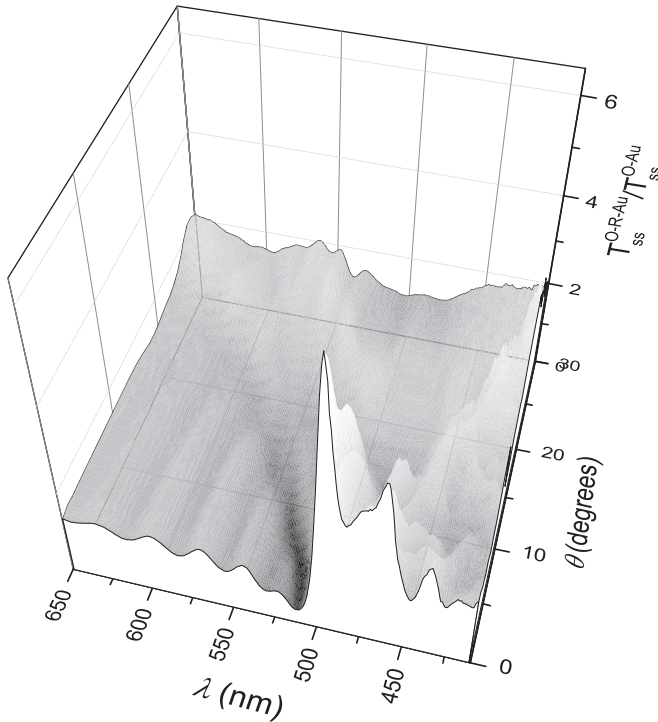


FIG. 13. Spectra of the interface function of the O-R-Au hybrid architecture in *s*-polarized light in the spectral range of the second harmonic of the resonator.

Hence, one can assume the same functionality of these hybrid architectures.

The squeezing of the transmission enhancement band along the increase of the number of diffracting layers is a direct consequence of the improved quality factor of the (111) diffraction resonance. The blueshift of this enhancement band is also consistent with the shift of the resonance wavelength of the effective microcavity.

The pronounced splitting of the transmission enhancement band is seen in the interface function spectra of the 9-layer O-R-Au hybrid at the avoided band crossing of (111) diffraction resonance with (200) and  $\bar{1}\bar{1}1$  ones. Remarkably, the 4-layer opal-based structure, which possesses only one

characteristic A-B-C-A sequence of (111) planes, shows the similar drop of the transmission enhancement. The avoided band crossing is less pronounced in this case because the diffraction resonances are essentially weak. This results in the broadening of the angle range of the split defect band transmission from 37–53° to 35–62°. Reasonably, no sign of avoided band crossing demonstrate the interface function spectra of 2-layer-based hybrid since no 3D lattice is formed in this colloidal coating.

**VIII. SUMMARY**

The reported experiments illustrate the feasibility of engineering the optical response of photonic crystals without changing their structure and composition, but solely through manipulations with the crystal environment. In the colloidal crystal, which is terminated by the metal mirror, one can expect the improvement of the light confinement and formation of the hybrid photonic-plasmonic modes. In turn, the interference of the transmitted and recycled light can be controlled by means of the external cavity. This strategy results in accomplishing the defect transmission band in the stop-band of photonic crystal, if the multiple- $2\pi$ -phase shift for the round trip in the hybrid structure is achieved at the stop-band wavelength.

The magnitude and the spectral resolution of the defect band depends on the quality factor of the Bragg resonance at (111) planes of the opal crystal. The width of the defect band can be reduced by increasing the number of diffracting planes in the Bragg mirror. However, this improvement is counteracted by the increase of the light scattering at intrinsic lattice defects. Nevertheless, the observed transmission increase in the hybrid opal equipped with the metal-mirrored cavity is by order of magnitude higher compared to the case of the similar cavity sandwiched between two opal crystals. A possible reason of such improvement is the higher degree of coherence of the transmitted and recycled light.

The 3D arrangement of diffracting planes in the opal mirror leads to the modification of the defect band appearance with respect to the 1D Bragg mirror, namely, to (i) the azimuth anisotropy of enhancement in accord to the symmetry of the lattice, (ii) the enhancement cancellation at the regions of the

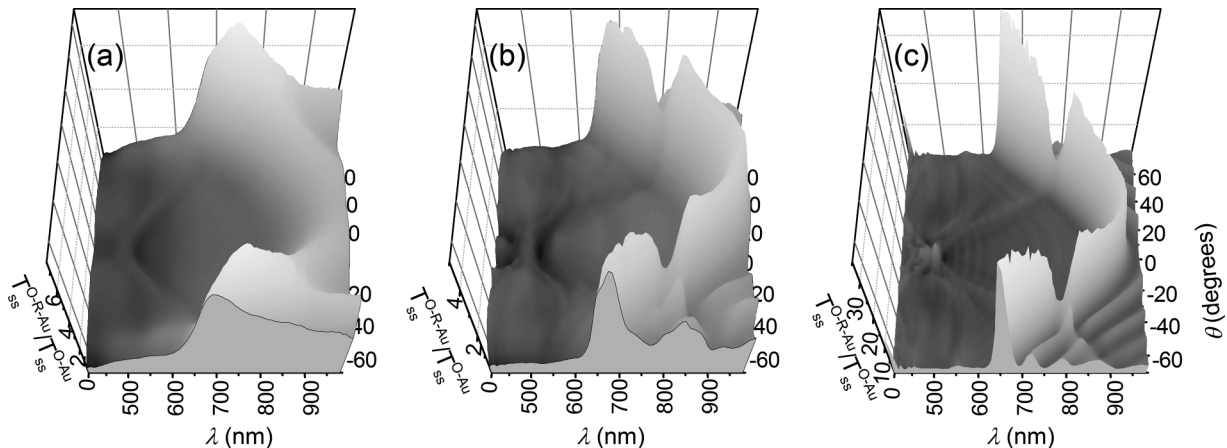


FIG. 14. Interface function spectra illustrating the evolution of the defect band of the O-R-Au architecture along the increase of the number of sphere monolayers in the colloidal crystal films. (a) 2(111)-R-Au hybrid, (b) 4(111)-R-Au hybrid, and (c) 9(111)-R-Au hybrid.

avoided band crossing, and (iii) the dependence on the field structure in diffracting Bloch modes at the band crossing.

Practical outcomes of presented investigation are (i) the introduction of the simple hybrid approach that bears a potential for attaining different PhC functionalities, (ii) the demonstration of the importance of preserving the coherence of light for the round trip in the structure with artificial defect, and (iii) the estimating of the quality factor of a defect band attainable with hybrid opal crystals. Since the hybrid method is not specific to colloidal photonic crystals, it can

be used as an enabling technology suitable for industrial up scaling.

## ACKNOWLEDGMENTS

This work was supported by the DFG Cluster of Excellence “Engineering of Advanced Materials” and EU IRSES project Phantasy. Authors are grateful to D. Ploß for taking SEM images.

\*Corresponding author: sergei.romanov@mpl.mpg.de

<sup>1</sup>J. D. Joannopoulos, S. G. Johnson, J. N. Winn, and R. D. Meade, *Photonic Crystals: Molding the Flow of Light*, 2nd ed. (Princeton University Press, Princeton, 2008), p. 304.

<sup>2</sup>X. Yu, L. Shi, D. Han, J. Zi, and P. V. Braun, *Adv. Funct. Mater.* **20**, 1 (2010).

<sup>3</sup>M. Lopez-García, J. F. Galisteo-Lopez, A. Blanco, J. Sanchez-Marcos, C. Lopez, and A. Garcia-Martin, *Small* **6**, 1757 (2010).

<sup>4</sup>S. G. Romanov, N. Vogel, K. Bley, K. Landfester, C. K. Weiss, S. Orlov, A. V. Korovin, G. P. Chuiko, A. Regensburger, A. S. Romanova, A. Kriesch, and U. Peschel, *Phys. Rev. B* **86**, 195145 (2012).

<sup>5</sup>P. V. Braun, S. A. Rinne, and F. García-Santamaría, *Adv. Mater.* **18**, 2665 (2006).

<sup>6</sup>A. Chutinan and S. John, *Phys. Rev. E* **71**, 026605 (2005).

<sup>7</sup>Y. Xia, B. Gates, Y. Yin, and Y. Lu, *Adv. Mater.* **12**, 693 (2000).

<sup>8</sup>A. van Blaaderen, R. Ruel, and P. Wiltzius, *Nature* **385**, 321 (1997).

<sup>9</sup>R. Rengarajan, P. Jiang, D. C. Larrabee, V. L. Colvin, and D. M. Mittleman, *Phys. Rev. B* **64**, 205103 (2001).

<sup>10</sup>F. Fleischhaker, A. C. Arsenault, J. Schmidtke, R. Zentel, and G. A. Ozin, *Chem. Mater.* **18**, 5640 (2006).

<sup>11</sup>P. Ferrand, M. Egen, J. Seekamp, R. Zentel, S. G. Romanov, and C. M. Sotomayor Torres, *Appl. Phys. Lett.* **83**, 5289 (2003).

<sup>12</sup>W. Lee, S. A. Pruzinsky, and P. V. Braun, *Adv. Mater.* **14**, 271 (2002).

<sup>13</sup>S. G. Romanov, H. M. Yates, M. E. Pemble, and R. M. De La Rue, *J. Phys.: Condens. Matter* **12**, 8221 (2000).

<sup>14</sup>E. Istrate and E. H. Sargent, *Rev. Mod. Phys.* **78**, 455 (2006).

<sup>15</sup>M. Egen, R. Voss, B. Griesebock, R. Zentel, S. Romanov, and C. Sotomayor Torres, *Chem. Mater.* **15**, 3786 (2003).

<sup>16</sup>E. Palacios-Lidón, J. E. Galisteo-López, B. H. Juárez, and C. López, *Adv. Mater.* **16**, 341 (2004).

<sup>17</sup>S. G. Romanov, A. Regensburger, A. V. Korovin, and U. Peschel, *Adv. Mater.* **23**, 2515 (2011).

<sup>18</sup>L. Shi, X. Liu, H. Yina, and J. Zi, *Phys. Lett. A* **374**, 1059 (2010).

<sup>19</sup>C. D. Dushkin, K. Nagayama, T. Miwa, and P. A. Kralchevsky, *Langmuir* **9**, 3695 (1993).

<sup>20</sup>V. G. Balakirev, V. N. Bogomolov, V. V. Zhuravlev, Y. A. Kumzerov, V. P. Petranovskii, S. G. Romanov, and L. A. Samoilovich, *Kristallografiya* **38**, 111 (1993) [*Crystallogr. Rep.* **38**, 348 (1993)].

<sup>21</sup>K. Iga, *IEEE J. Sel. Top. Quantum Electron.* **6**, 1201 (2000).

<sup>22</sup>E. Istrate and E. H. Sargent, *Appl. Phys. Lett.* **86**, 151112 (2005).

<sup>23</sup>H. M. van Driel and W. L. Vos, *Phys. Rev. B* **62**, 9872 (2000).

<sup>24</sup>S. G. Romanov, T. Maka, C. M. Sotomayor Torres, M. Müller, R. Zentel, D. Cassagne, J. Manzanares-Martinez, and C. Jouanin, *Phys. Rev. E* **63**, 056603 (2001).

<sup>25</sup>W. Khunsin, A. Amann, G. Kocher-Oberlehner, S. G. Romanov, S. Pullteap, H. C. Seat, E. P. O'Reilly, R. Zentel, and C. M. Sotomayor Torres, *Adv. Funct. Mater.* **22**, 1812 (2012).

<sup>26</sup>G. M. Gajiev, V. G. Golubev, D. A. Kurdyukov, A. V. Medvedev, A. B. Pevtsov, A. V. Sel'kin, and V. V. Travnikov, *Phys. Rev. B* **72**, 205115 (2005).

<sup>27</sup>S. G. Romanov, U. Peschel, M. Bardosova, S. Essig, and K. Busch, *Phys. Rev. B* **82**, 115403 (2010).

<sup>28</sup>J. Nikoma, R. Loudon, and D. R. Tilley, *J. Phys.: Solid State Phys.* **7**, 3547 (1974).

<sup>29</sup>B. R. Cooper, H. Ehrenreich, and H. R. Philipp, *Phys. Rev. A* **138**, 494 (1965).

<sup>30</sup>S. G. Romanov, *Physics Solid State* **49**, 536 (2007).

<sup>31</sup>K. Wostyn, Y. Zhao, G. de Schaezen, L. Hellemans, N. Matsuda, K. Clays, and A. Persoons, *Langmuir* **19**, 4465 (2003).

<sup>32</sup>A. S. Romanova, A. V. Korovin, and S. G. Romanov, *Physics Solid State* **55**, 1725 (2013).

<sup>33</sup>J. Küchenmeister, C. Wolff, K. Busch, U. Peschel, and S. G. Romanov (unpublished).

<sup>34</sup>A. Yariv and P. Yeh, *Propagation and Control of Laser Radiation* (Wiley, New York, 1984).

<sup>35</sup>Y. Kurokawa, H. Miyazaki, and Y. Jimba, *Phys. Rev. B* **69**, 155117 (2004).

<sup>36</sup>R. M. Cole, Y. Sugawara, J. J. Baumberg, S. Mahajan, M. Abdelsalam, and P. N. Bartlett, *Phys. Rev. Lett.* **97**, 137401 (2006).

<sup>37</sup>S. G. Romanov, M. Bardosova, I. Povey, M. Pemble, and C. M. Sotomayor Torres, *Appl. Phys. Lett.* **92**, 191106 (2008).

<sup>38</sup>W. Khunsin, G. Kocher, S. G. Romanov, and C. M. Sotomayor Torres, *Adv. Funct. Mater.* **18**, 2471 (2008).